











# The *Magellan* Evolution of Galaxies Spectroscopic and Ultraviolet Reference Atlas (MegaSaura). II. Stacked Spectra

J. R. Rigby<sup>1</sup> , M. B. Bayliss<sup>2</sup> , J. Chisholm<sup>3</sup> , R. Bordoloi<sup>2,10</sup> , K. Sharon<sup>4</sup> , M. D. Gladders<sup>5,6</sup>, T. Johnson<sup>4</sup> ,  
R. Paterno-Mahler<sup>4</sup>, E. Wuyts<sup>7</sup> , H. Dahle<sup>8</sup> , and A. Acharyya<sup>9</sup>

<sup>1</sup> Observational Cosmology Lab, Goddard Space Flight Center, 8800 Greenbelt Road, Greenbelt, MD 20771, USA; [Jane.Rigby@nasa.gov](mailto:Jane.Rigby@nasa.gov)

<sup>2</sup> MIT Kavli Institute for Astrophysics and Space Research, 77 Massachusetts Avenue, Cambridge, MA 02139, USA

<sup>3</sup> Observatoire de Genève, Université de Genève, 51 Ch. des Maillettes, 1290 Versoix, Switzerland

<sup>4</sup> Department of Astronomy, University of Michigan, 500 Church Street, Ann Arbor, MI 48109, USA

<sup>5</sup> Department of Astronomy & Astrophysics, University of Chicago, 5640 S. Ellis Avenue, Chicago, IL 60637, USA

<sup>6</sup> Kavli Institute for Cosmological Physics, University of Chicago, 5640 South Ellis Avenue, Chicago, IL 60637, USA

<sup>7</sup> ArmenTeKort, Antwerp, Belgium

<sup>8</sup> Institute of Theoretical Astrophysics, University of Oslo, P.O. Box 1029, Blindern, NO-0315 Oslo, Norway

<sup>9</sup> The Australian National University, Australia

Received 2017 June 27; revised 2017 October 18; accepted 2017 October 20; published 2018 January 25

## Abstract

We stack the rest-frame ultraviolet spectra of  $N = 14$  highly magnified gravitationally lensed galaxies at redshifts  $1.6 < z < 3.6$ . The resulting new composite spans  $900 < \lambda_{\text{rest}} < 3000 \text{ \AA}$ , with a peak signal-to-noise ratio (S/N) of 103 per spectral resolution element ( $\sim 100 \text{ km s}^{-1}$ ). It is the highest S/N, highest spectral resolution composite spectrum of  $z \sim 2\text{--}3$  galaxies yet published. The composite reveals numerous weak nebular emission lines and stellar photospheric absorption lines that can serve as new physical diagnostics, particularly at high redshift with the *James Webb Space Telescope* (*JWST*). We report equivalent widths to aid in proposing for and interpreting *JWST* spectra. We examine the velocity profiles of strong absorption features in the composite, and in a matched composite of  $z \sim 0$  COS/*HST* galaxy spectra. We find remarkable similarity in the velocity profiles at  $z \sim 0$  and  $z \sim 2$ , suggesting that similar physical processes control the outflows across cosmic time. While the maximum outflow velocity depends strongly on ionization potential, the absorption-weighted mean velocity does not. As such, the bulk of the high-ionization absorption traces the low-ionization gas, with an additional blueshifted absorption tail extending to at least  $-2000 \text{ km s}^{-1}$ . We interpret this tail as arising from the stellar wind and photospheres of massive stars. Starburst99 models are able to replicate this high-velocity absorption tail. However, these theoretical models poorly reproduce several of the photospheric absorption features, indicating that improvements are needed to match observational constraints on the massive stellar content of star-forming galaxies at  $z \sim 2$ . We publicly release our composite spectra.

**Key words:** galaxies: evolution – galaxies: high-redshift – gravitational lensing: strong – intergalactic medium – stars: winds, outflows

**Supporting material:** tar.gz file

## 1. Introduction

The rest-frame ultraviolet spectra of galaxies are particularly rich in diagnostics of hot stars, the nebulae they ionize, and the outflowing winds they power. The *International Ultraviolet Explorer*, the *Far Ultraviolet Spectroscopic Explorer*, the *Hopkins Ultraviolet Telescope*, and four generations of ultraviolet spectrographs on board *The Hubble Space Telescope* have studied these diagnostics in nearby galaxies (e.g., Kinney et al. 1993; Heckman et al. 2011; Leitherer et al. 2011; Crowther et al. 2016). As most of the universe’s stellar mass was formed at  $z \sim 2\text{--}3$  during an era of rampant star formation (compare to today at  $z \sim 0$ ), it is natural to compare the rest-frame UV spectra of  $z \sim 0$  and  $z \sim 2\text{--}3$  galaxies. Do distant galaxies have the same populations of massive stars as nearby galaxies? Have galactic winds evolved with time?

Obtaining such diagnostic spectra for normal galaxies at redshifts of  $1 < z < 4$  is normally beyond the reach of current instrumentation, and indeed, is a goal of future mission concepts such as a large ultraviolet/optical/infrared

telescope or “LUVOIR” (Kouveliotou et al. 2014; Dalcanton et al. 2015). Progress has been made by stacking low-resolution spectra ( $R \sim 600\text{--}1400$ ) of galaxies at these redshifts, to study spectral features too faint to be detected in individual spectra.

Shapley et al. (2003) stacked the low-signal-to-noise Keck/LRIS spectra of almost 1000 faint Lyman break galaxies at redshifts of  $z \sim 2\text{--}3$ . Jones et al. (2012) extended this analysis to  $z \sim 4$  by stacking the Keck/DEIMOS spectra of  $N = 81$  Lyman break galaxies. Steidel et al. (2010) stacked the Keck/LRIS spectra of galaxies at  $z \sim 2.3$ , and Steidel et al. (2016) stacked the Keck/LRIS spectra of 30 star-forming galaxies at  $z = 2.4$ . These latter two studies also stacked rest-frame optical spectra from Keck/NIRSPEC or Keck/MOSFIRE for the same samples, enabling cross-comparison of the rest-frame ultraviolet and optical emission lines. Zhu et al. (2015) stacked spectra of 8620 emission-line galaxies at  $0.6 < z < 1.2$ , covering to longer wavelengths ( $\lambda_r > 2200 \text{ \AA}$ ). Table 1 summarizes the basic parameters of the composites that resulted from these studies—redshift range, wavelength range, spectral resolving powers, and signal-to-noise ratio (S/N).

<sup>10</sup> Hubble Fellow.

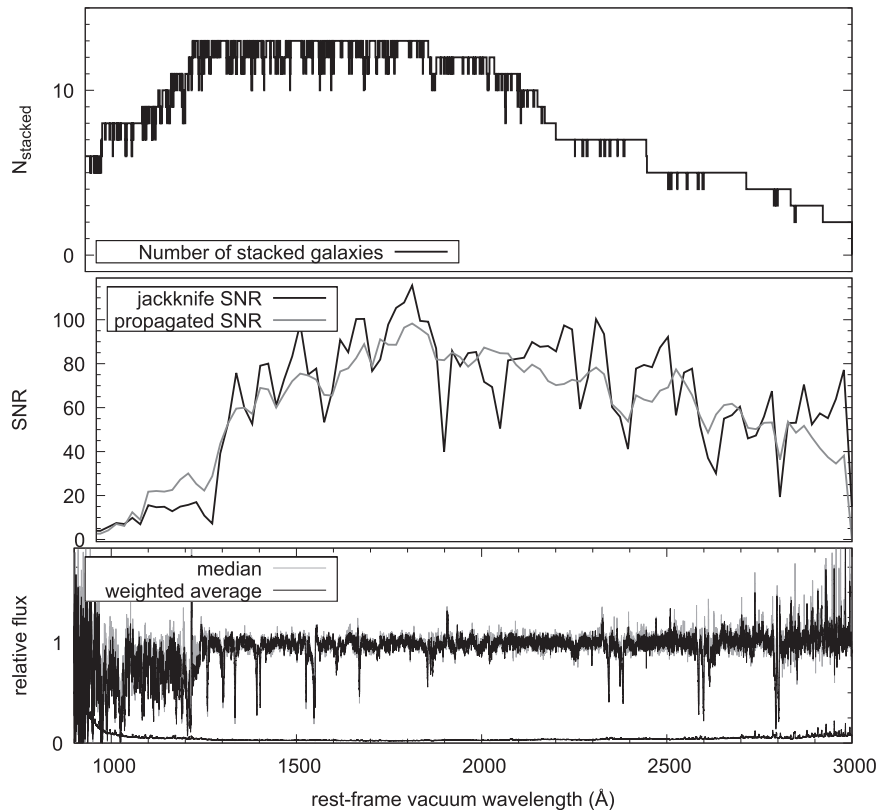


**Figure 1.** MEGaSaURA shape-normalized stacked spectrum. The top panel shows the number of galaxies that went into the stack at each rest-frame wavelength; that number is affected by the observed wavelength coverage of the input spectra, the location of saturated skylines, and the expected positions of intervening absorption lines. The middle panel shows two independent measures of the S/N, per resolution element, of the weighted average stacked spectrum: the jackknife uncertainty and the propagation of the individual uncertainty spectra. The S/N curves have been smoothed for readability. The bottom panel compares two realizations of the shape-normalized stack: the weighted average (black) to the median (gray).

**Table 1**  
Comparison of the MEGaSaURA Stacked Spectrum to Other Templates

Spectrum	$N_{\text{stacked}}$	$z$	$\lambda_{\text{rest}}$ range (Å)	$R$	$S/N_{\text{peak}}$
MEGaSaURA MagE stack (this paper)	14	$1.68 < z < 3.6$	900–3000	$\sim 3300$	103
Shapley et al. (2003) composite	811	$2.4 < z < 3.5$	920–2000	$\sim 560$	$114^{\text{a}}$
Jones et al. (2012) composite	81	$3.5 < z < 4.5$	1000–1800	$\sim 660$	30
Steidel et al. (2010) composite	89, 102	$2.3 \pm 0.3$	1000–1600	800, 1330	...
Steidel et al. (2016) composite	30	$2.4 \pm 0.11$	1000–2200	1400	38
cB58, Pettini et al. (2002)	1	2.7276	1075–2500	5200	55
eBOSS, Zhu et al. (2015)	8620	$0.6 < z < 1.2$	2200–7500	$\sim 2000$	$70^{\text{b}}$
Stack of Chisholm et al. (2016) (this paper)	41	0.0–0.25	1150–1780	$3300^{\text{c}}$	150

**Note.** Columns: (1) source of template spectrum; (2) number of galaxies that went into the template; (3) redshift range; (4) rest-frame wavelength range; (5) spectral resolving power, defined as  $R \equiv \delta\lambda/\lambda$ , where  $\delta\lambda$  is the full width at half maximum; (6) peak S/N of the continuum, per resolution element.

<sup>a</sup> S/N not given in the paper; we have estimated it as the square root of the sample size, times the quoted average S/N of the input spectra.

<sup>b</sup> S/N at 2500–3000 Å.

<sup>c</sup> The spectral resolution of the COS spectra varies with galaxy morphology. As described in the text, for each input galaxy, we measured the effective spectral resolution from Milky Way absorption lines, then convolved with a Gaussian and rebinned, to produce an effective spectral resolution for the COS stack of  $R = 3300$ .

In this paper, we stack the spectra of  $N = 14$  gravitationally lensed galaxies from Project MEGaSaURA: the *Magellan* Evolution of Galaxies Spectroscopic and Ultraviolet Reference Atlas (Rigby et al. 2018; hereafter Paper I). The resulting stacked spectra represent a new moderate spectral resolution, rest-frame ultraviolet composite for star-forming galaxies at  $z \sim 2$ . The high S/N of this composite enables a detailed comparison with with stellar population synthesis

models, enabling us to constrain the stellar and galactic winds.

All magnitudes quoted are in the AB system.

## 2. Methods

Below, we describe the spectra that are stacked to generate the MagE MEGaSaURA composite spectra, the methodology for measuring the systemic redshifts, the methodology for

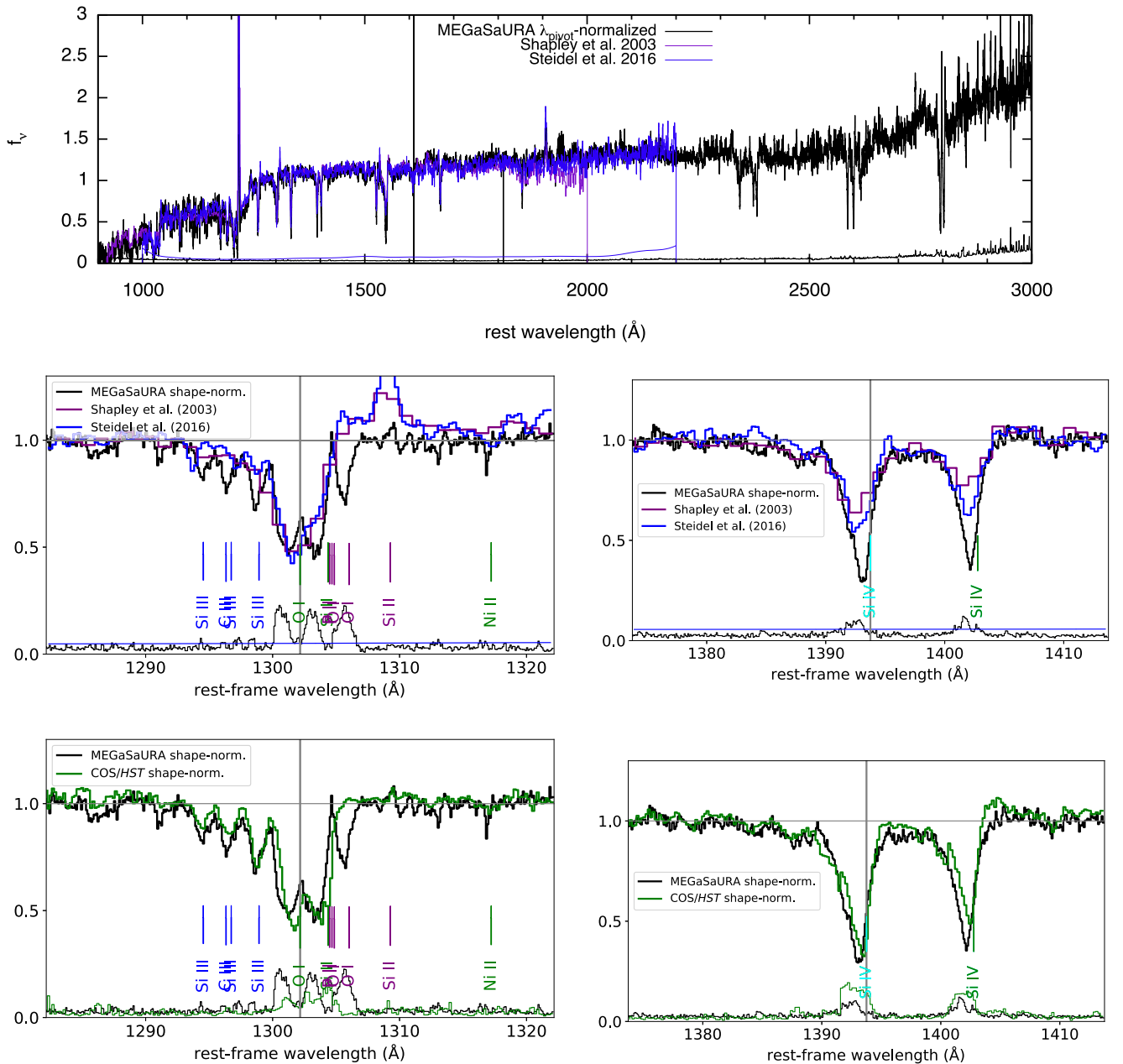


**Figure 2.** The top panel shows a comparison of the MEGaSaURA  $\lambda_{\text{pivot}}$ -normalized stacked spectrum (black steps) to previously published templates: the composite spectra of Shapley et al. (2003) (purple steps) and Steidel et al. (2016) (blue steps). Each plotted spectrum has been renormalized by dividing the flux density by the median in the range  $1267 < \lambda_r < 1276$  Å. Propagated uncertainty spectra are plotted with the same color scheme as the spectra. The middle panels zoom in on the templates for two spectral regions of interest. The left middle panel shows the complex spectral region near 1300 Å that includes multiple photospheric absorption lines of Si III and C III, O I 1302 ISM absorption, and Si II 1309 fine structure emission. The right middle panel shows the region near the Si IV doublet. Vertical ticks and labels mark features of interest, color-coded as photospheric absorption (blue), interstellar medium (ISM) (green), and stellar winds (cyan). The bottom panels show the same spectral regions as the middle panels, but now comparing the megasaura shape-normalized stack (black steps) to the COS/HST  $z \sim 0$  stack (green steps). Compared to previous templates, the higher spectral resolution MEGaSaURA stack much more clearly detects weak features like the photospheric absorption lines.

normalizing the fluxes of the input spectra, and the methodology for stacking the spectra. For reasons detailed in Section 2.3, rather than generating a single composite MEGaSaURA spectrum, we create several different stacks, each with different methods for normalizing the input spectra. We describe how we stacked COS/HST spectra of  $z \sim 0$  galaxies to make a composite spectrum representing local galaxies. We also describe the method of measuring outflow velocities.

### 2.1. Input MEGaSaURA MagE Spectra

The MEGaSaURA sample and MagE spectra are described in detail in Paper I. The  $N = 15$  galaxies span the redshift range  $1.6 < z < 3.6$  and are among the brightest lensed sources selected from the Sloan Digital Sky Survey; the brightest have a  $g$ -band magnitude of  $g_{AB} \lesssim 21$ . By selection, the MEGaSaURA galaxies are skewed toward galaxies with high rest-frame UV surface brightness, i.e., vigorously star-forming galaxies with relatively low dust content. We are





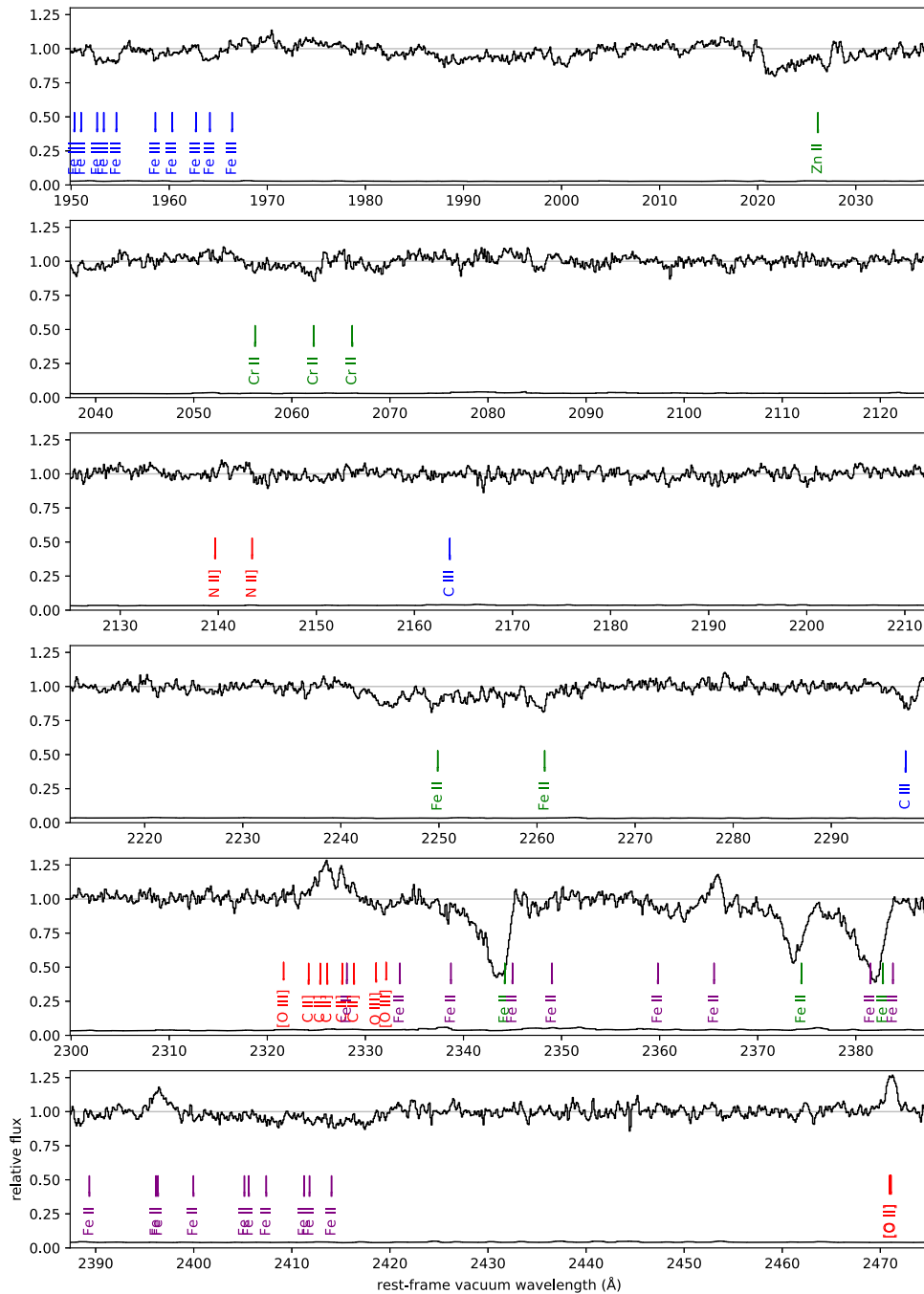


Figure 3. (Continued.)

light-weighted stellar age is 10 Myr. The theoretical stellar continuum models were compiled using the WM-BASIC code (Leitherer et al. 1999, 2010) with the Geneva stellar evolution tracks with high mass loss (Meynet et al. 1994). We used a Kroupa IMF, with a power-law index of 1.3 (2.3) for the low (high) mass slope, and a high-mass cut-off at  $100 M_{\odot}$ . We fully discuss these models in an upcoming paper (J. R. Rigby et al. 2018, in preparation). Given this method of fitting the stellar continuum, the stellar redshift is dominated by the myriad weak photospheric absorption features. The nebular redshift was measured by fitting two Gaussians to the [C III] 1907, C III] 1909 Å doublet, except as noted in

Table 3 of Paper I. We noted in Paper I that there is no systematic offset between the redshifts of the hot stars and the nebulae; the median offset and median absolute deviation are  $-1 \pm 31 \text{ km s}^{-1}$ .

We experimented with the choice of systemic redshift for the stacks: nebular or stellar. Unsurprisingly, the nebular emission lines are narrower when the nebular redshifts were used as systemic. The line profiles of the photospheric absorption lines near  $\lambda_{\text{rest}} = 1300 \text{ Å}$  are similar for the two choices of systemic redshift. As the nebular redshifts are more precise, we use the nebular redshifts as the systemic redshifts for all the stacks of the MEGaSURA spectra.

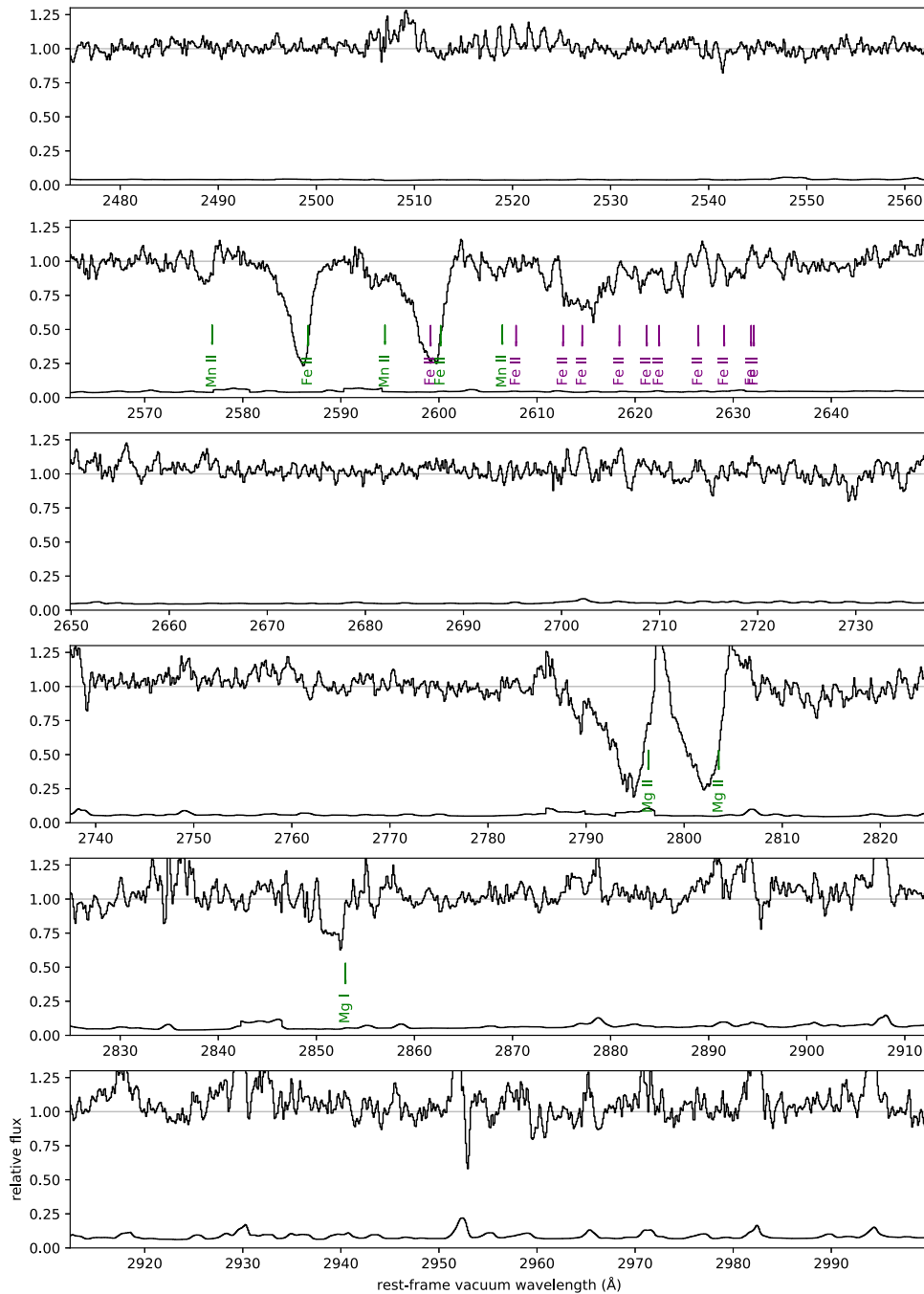


Figure 3. (Continued.)

### 2.3. Normalization of Input Spectra

Before stacking, we normalize each spectrum, using one of the following methods:

1. Divide each input spectrum by its hand-fit spline continuum from Paper I. This normalizes both the zeropoint and shape of each input spectrum and prevents the stack from “ringing” at the edges of the bandpass, due to small numbers statistics and a range of spectral slopes. The output spectrum should have a flat spectral shape, with the exception of the region near and blueward of Ly $\alpha$ , where continuum fitting is extremely challenging.

This stack is best suited for measuring the equivalent widths of faint emission lines, as for this application the galaxy’s intrinsic spectral shape is not important. It can also be used to study absorption features from the interstellar medium (ISM). We call the composite spectrum that results from this method the shape-normalized stack.

2. Divide each input spectrum by the median flux density within a pivot wavelength range:  $1267 < \lambda_r < 1276 \text{ \AA}$ . This region was chosen because it is centrally located in the spectra and contains relatively few spectral features. This normalization affects only the zeropoint of each

**Table 2**  
Emission Lines

Line	$\lambda_{\text{vac}}$ (Å)	$W_r$ (Å)	Uncertainty $W_r$ (Å)	Significance
C III 977	977.0200	>−0.1461	...	...
He II 1084	1084.9420	>−0.0758	...	...
Ly $\alpha$	1215.6700	−1.2654	0.04	50.65
O I 1304	1304.8576	>−0.0352	...	...
O I* 1306	1306.0286	>−0.0348	...	...
Si II 1309	1309.2757	−0.2441	0.02	21.26
C II 1335a	1334.5770	>−0.031	...	...
C II* 1335b	1335.6630	>−0.0349	...	...
C II* 1335c	1335.7080	>−0.035	...	...
N II] 1430	1430.4100	>−0.0306	...	...
N II]1431	1430.9730	>−0.0306	...	...
N IV] 1486	1486.5000	−0.0428	0.02	4.12
Si II* 1533	1533.4312	−0.0367	0.01	3.41
He II 1640 broad	1640.4170	−0.98	0.1	−
He II 1640 narrow	1640.4170	>−0.22	...	...
O III] 1660	1660.8090	−0.0634	0.01	6.37
O III] 1666	1666.1500	−0.1716	0.02	13.98
N III] 1750	1749.7000	>−0.0286	...	...
Si III] 1882	1882.7070	−0.0673	0.01	5.70
Si III] 1892	1892.0290	>−0.0357	...	...
[C III] 1906	1906.6800	−0.5214	0.02	38.37
C III] 1908	1908.7300	−0.3956	0.02	30.26
N II] 2140	2139.6800	−0.0649	0.02	4.46
[O III] 2320	2321.6640	>−0.0571	...	...
C II] 2323	2324.2140	>−0.0533	...	...
C II] 2325c	2326.1130	−0.4034	0.09	19.61
C II] 2325d	2327.6450	−0.2055	0.07	10.35
C II] 2328	2328.8380	−0.064	0.04	3.17
Si II] 2335a	2335.1230	>−0.0608	...	...
Si II] 2335b	2335.3210	>−0.0625	...	...
Fe II* 2365	2365.5520	−0.183	0.02	9.40
Fe II* 2396a	2396.1497	>−0.0578	...	...
Fe II* 2396b	2396.3559	>−0.0576	...	...
[O II] 2470	2471.0270	−0.3584	0.02	18.77
Fe II* 2599	2599.1465	>−0.0596	...	...
Fe II* 2607	2607.8664	>−0.0659	...	...
Fe II* 2612	2612.6542	>−0.0665	...	...
Fe II* 2614	2614.6051	>−0.0575	...	...
Fe II* 2618	2618.3991	>−0.0632	...	...
Fe II* 2621	2621.1912	>−0.0627	...	...
Fe II* 2622	2622.4518	>−0.0676	...	...
Fe II* 2626	2626.4511	>−0.0656	...	...
Fe II* 2629	2629.0777	>−0.068	...	...
Fe II* 2631	2631.8321	>−0.0672	...	...
Fe II* 2632	2632.1081	>−0.0655	...	...
Mg II 2797b	2798.7550	−0.367	0.04	14.58
Mg II 2797d	2803.5310	−0.3522	0.04	14.20
He I 2945	2945.1030	>−0.1063	...	...

**Note.** Rest-frame ultraviolet emission lines in the shape-normalized stacked spectrum. Columns are: (1) line identification, (2) vacuum wavelength (Å), (3) measured rest-frame equivalent width (Å) (with negative sign indicating absorption), (4) uncertainty on the previous column, and (5) significance of the detected feature, in  $\sigma$ , according to the Schneider et al. (1993) significance criterion. Non-detections are quoted as  $3\sigma$  limits. Note: The C II 232X complex is challenging to fit given the close spacing of the four emission lines. The total equivalent width of the complex is well-measured, at  $W_r = -0.68 \pm 0.14$ , but the fit is degenerate as to which components contain most of the flux. We therefore fit the complex by fixing the relative strengths of the lines to the predictions of MAPPINGS V.

input spectrum and preserves the spectral shape. As a result, when spectra with very different slopes are averaged, the output spectrum may show “ringing” at wavelengths far from the pivot wavelength where the spectra were normalized. As this stack preserves spectral shape, it is the stack to which we can fit stellar population synthesis models. We call the composite spectrum that results from this method the  $\lambda_{\text{pivot}}$ -normalized stack.

3. Divide each input spectrum by its best-fit model linear combination of Starburst 99 models from J. R. Rigby et al. (2018, in preparation). This normalization affects both the zeropoint and the spectral shape. This stack may be the best for analyzing ISM absorption profiles, as the stellar wind features have already been removed. We call the composite spectrum that results from this method the S99-normalized stack.

#### 2.4. Stacking Methodology

We stack the MEGaSaURA spectra of  $N = 14$  gravitationally lensed galaxies as follows. Each input spectrum is continuum-normalized using one of the three normalization methods described above. We then shift it to its rest frame, using the nebular line redshift as the systematic redshift. We then resample, using linear interpolation, onto a common output wavelength grid with a sampling of 0.1 Å.

We take steps to keep the composite spectra free of spurious features due to intervening absorption systems. We identified such systems through a systematic search for intervening Mg II, C IV, and Si IV doublets in all MEGaSaURA spectra. In each input spectrum, we mask  $\pm 200$  km s $^{-1}$  around the positions of all transitions from these intervening absorption systems.

The input spectra, after having been continuum-normalized, de-redshifted, resampled, and masked of intervening absorption systems, are then stacked using two methods: weighted average (weighted by the uncertainty spectra), and median (with no weighting). For most applications, the weighted average is preferable to the median, as it has higher S/N.

To understand the uncertainty in the composite spectra, we perform jackknife tests, in which we compute the weighted average  $n$  times, each with a different spectrum masked out. For each stack, we compute two estimates of the per-pixel uncertainty: (a) the uncertainty spectrum propagated from the individual uncertainty spectra, and (b) the jackknife uncertainty  $\sigma_{\text{jackknife}}$ , which measures the variation in the  $n$  jackknife spectra:

$$\sigma_{\text{jackknife}}^2 = \frac{(n-1)}{n} \sum_{i=1}^n (x_i - x_{(\cdot)})^2, \quad (1)$$

where  $x_i$  is the pixel value in the  $i$ th jackknife spectrum, and  $x_{(\cdot)}$  is the pixel value in the weighted average spectrum. These two uncertainty estimates, which should be independent, are consistent, as Figure 1 illustrates. Used together, the median spectra and the jackknife uncertainty spectra can be used to check whether a particular spectral feature is unduly influenced by a single galaxy.

#### 2.5. Stacking COS/HST Spectra

To enable an apples-to-apples comparison of the MagE MEGaSaURA stack to the spectra of galaxies in the nearby universe, we stack the spectra of  $z \sim 0$  galaxies with COS/HST spectra using the G130M and G160M gratings from



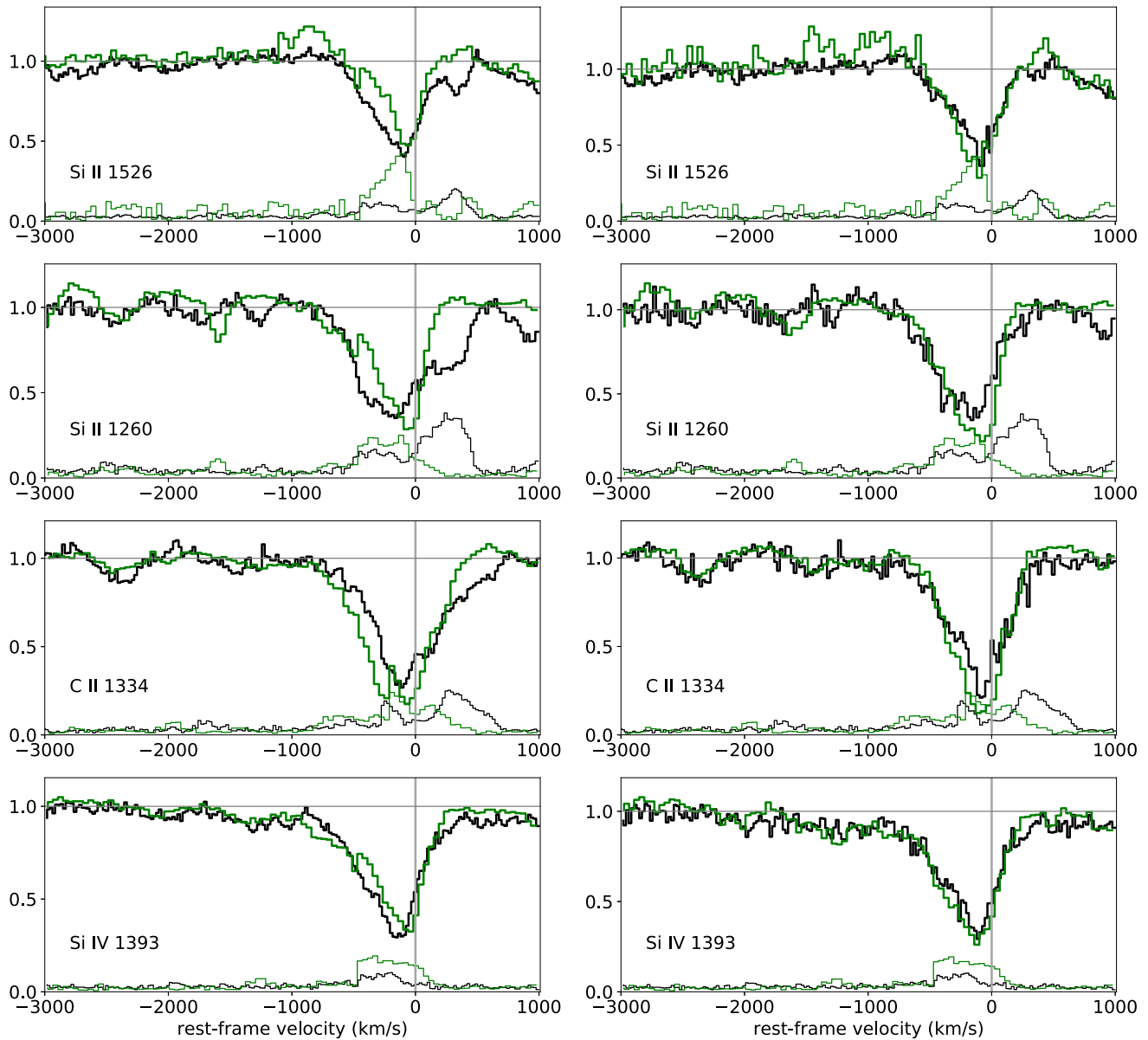


**Figure 4.** Comparison of the velocity profiles of strong absorption features at two cosmic epochs: at  $z \sim 2$  from the shape-normalized weighted-average MEGaSaURA stack (black steps) and our stack of  $z \sim 0$  *HST*/COS spectra (green steps) from Chisholm et al. (2016). The left panel shows the weighted average for each stack; the right panel shows the median. In all cases, we plot the jackknife uncertainty as the uncertainty spectrum. Excess variance is seen at the locations of Si II\* 1264 and C II\* 1335. The velocity profiles of the  $z \sim 2$  stack are very similar to that of the  $z \sim 0$  stack. The input spectra were continuum-normalized before stacking, so unity represents zero absorption.

Chisholm et al. (2016). That local sample is comprised of 41 galaxies<sup>11</sup> with star formation rates of  $0.01\text{--}137 M_{\odot} \text{ yr}^{-1}$ . Each galaxy has blueshifted ISM absorption lines at the  $1\sigma$  significance level. The stack represents the most complete sample of local star-forming galaxies with COS/*HST* spectra that show galactic outflows.

The input COS spectra requires extra pre-processing. We mask the expected wavelengths of geocoronal and Milky Way emission lines. The spectral resolution of COS is higher than that of MagE: for a point source, it is  $R = 16000$ , but it decreases as emission fills the circular aperture of COS. In the COS spectra we are stacking, the Milky Way absorption lines

indicate effective spectral resolutions ranging from  $R = 4000$  to  $R = 14000$ , with a median of  $R = 9000$  due to the diffuse, extended morphology of these galaxies in the slit. Therefore, we resample the wavelength grid of each input COS spectrum to be Nyquist sampled for the spectral resolution measured from the Milky Way absorption lines, then convolve by a Gaussian kernel to lower the spectral resolution to that of MagE ( $R = 3300$ ), and then resample the wavelength array once more, to be Nyquist sampled at  $R = 3300$ . Downgrading the effective spectral resolution in this way does not meaningfully change the profiles of absorption lines in the stacked spectrum, but it does change the per-pixel S/N, and as such, the measured maximum velocity.

Given the large number of COS spectra, rather than fit the continuum by hand as for the MagE spectra, we fit the continuum automatically, by masking spectral features and then

<sup>11</sup> We dropped one galaxy, M83 1, from the stack due to difficulty fitting its continuum; this galaxy has extremely high super-solar metallicity, unlike the MEGaSaURA sample.

**Table 3**  
Absorption Velocity Measurements

transition	IP (eV)	$v_{\text{mean}}$ (km s <sup>-1</sup> )	$\sigma$ (km s <sup>-1</sup> )	$v_{\text{max}}$ (km s <sup>-1</sup> )	$\sigma$ (km s <sup>-1</sup> )	$v_{\text{mean}}$ (km s <sup>-1</sup> )	$\sigma$ (km s <sup>-1</sup> )	$v_{\text{max}}$ (km s <sup>-1</sup> )	$\sigma$ (km s <sup>-1</sup> )
MEGASaURA MagE/Magellan shape-normalized stack									
Measurements of weighted average stack					Measurements of median stack				
O I 1302	13.6	...	...	< -500 <sup>a</sup>	...	...	...	< -500 <sup>a</sup>	...
Mg II 2796	15.0	-310	3	-885	0	-271	10	-721	72
Fe II 2344	16.2	-225	20	-965	111	-178	15	-741	50
Fe II 2383	16.2	...	...	< -840 <sup>b</sup>	...	...	...	< 840 <sup>b</sup>	...
Si II 1260	16.35	-97	1	-772	37	-203	1	-740	24
Si II 1526	16.35	-92	1	-632	30	-138	4	-606	39
Al II 1670	18.8	-128	18	-707	40	-145	34	-634	27
C II 1334	24.4	-53	13	-938	183	-163	25	-971	227
Al III 1854	28.4	-568	136	-2268	494	-275	148	-984	513
Si IV 1393	45.1	-260	76	-1327	406	-419	67	-2097	290
C IV 1548	64.49	-517	43	-2696	159	-535	41	-2513	150
COS/HST R = 3300 shape-normalized stack									
Measurements of weighted average stack					Measurements of median stack				
O I 1302	13.6	...	...	< -500 <sup>a</sup>	...	...	...	< -500	...
Si II 1260	16.35	-189	6.0	-815	20	-179	6	-906	48
Si II 1526	16.35	-107	3.0	-574	0	-114	0	-532	0
Al II 1670	18.8	-64	34.0	-431	51	-88	61	-399	0
C II 1334	24.4	-191	17.0	-1561	86	-104	2	-684	34
Si IV 1393	45.1	-345	49.0	-1833	329	-371	10	-1733	51
C IV 1548	64.5	-355	27.0	-2386	172	-516	28	-2441	154

**Note.** Columns are: (1) line label; (2) ionization potential in electron volts; (3) absorption-weighted mean velocity  $v_{\text{mean}}$  for the weighted average stack; (4) uncertainty in  $v_{\text{mean}}$ ; (5) maximum velocity  $v_{\text{max}}$  for the weighted average stack; (6) uncertainty in  $v_{\text{max}}$ ; and (7)–(10) same as (3)–(6) but for the median stack. N V 1238 is not listed because absorption was not clearly detected.

<sup>a</sup> Blend with photospheric absorption.

<sup>b</sup> Blend with Fe II 2374 absorption.

convolving with a boxcar. Tests using the individual MagE spectra show that this automatic continuum fitting process produces continua that closely track our hand-fit continua. We then stacked the COS shape-normalized input spectra in the same way as we stacked the MagE spectra. The result is a shape-normalized COS stacked spectrum whose spectral resolution and S/N closely match that of the MagE stack (as quantified in Table 1).

### 2.6. Velocity Measurements

We compute two metrics of the absorption line velocity profiles: the maximum blueshifted velocity  $v_{\text{max}}$  and the absorption-weighted mean velocity  $v_{\text{mean}}$ . We used the weighted-average, shape-normalized stack to measure these metrics, for both the MagE stack and the COS stack.

We calculate the absorption-weighted mean velocity of the absorption line,  $v_{\text{mean}}$ , within the interval from  $v_{\text{max,blue}}$  to  $v_{\text{max,red}}$ . We restrict  $v_{\text{max,red}} < 600$  km s<sup>-1</sup> to prevent runaway fits in the case of doublets and other closely spaced absorption lines (for example, for C IV 1548).

Steidel et al. (2010) defined  $v_{\text{max}}$  as the velocity where the blue wing of the absorption returns to the continuum, specifically the first pixel to return. We adopt this definition for both  $v_{\text{max,blue}}$  and  $v_{\text{max,red}}$ , with a caveat to the reader that this metric is sensitive to the S/N and dispersion of the spectrum. This is indeed why, when we stack the  $z \sim 0$  COS/HST spectra, we downgrade the resolution to create a

stack with similar spectral resolution and noise properties to the MagE stack.

To gauge the uncertainty in  $v_{\text{max}}$  and  $v_{\text{mean}}$ , we scale the continuum by a factor over the range  $\pm 2\%$  (as this seemed the maximum plausible error in the continuum), measure the mean and maximum velocities each time, and quote the mean value and standard deviation.

### 2.7. Measuring Equivalent Widths

We measure the equivalent widths of emission lines in the shape-normalized stacked spectrum using the following methodology. We fit each group of neighboring spectral lines simultaneously, with one Gaussian per feature, using the nonlinear least-squares method as implemented in the Python tool `scipy.optimize.curve_fit`. Neighboring lines are defined as being separated by  $\leq 5$  spectral resolution elements. We use the equivalent width significance criterion of Schneider et al. (1993).

## 3. Results

### 3.1. The Stacked Spectra

The stacked spectra span a rest-frame wavelength range of  $900 < \lambda_{\text{rest}} < 3000$  Å, with 0.1 Å pixels. We calculate the median S/N per resolution element in four regions that are free of spectral lines: S/N = 76 for 1440–1450 Å, S/N = 92 for 1460–1470 Å, S/N = 79 for 1680–1700 Å, and S/N = 101 for 1760–1800 Å. Figure 1 plots the stacked spectrum, the S/N

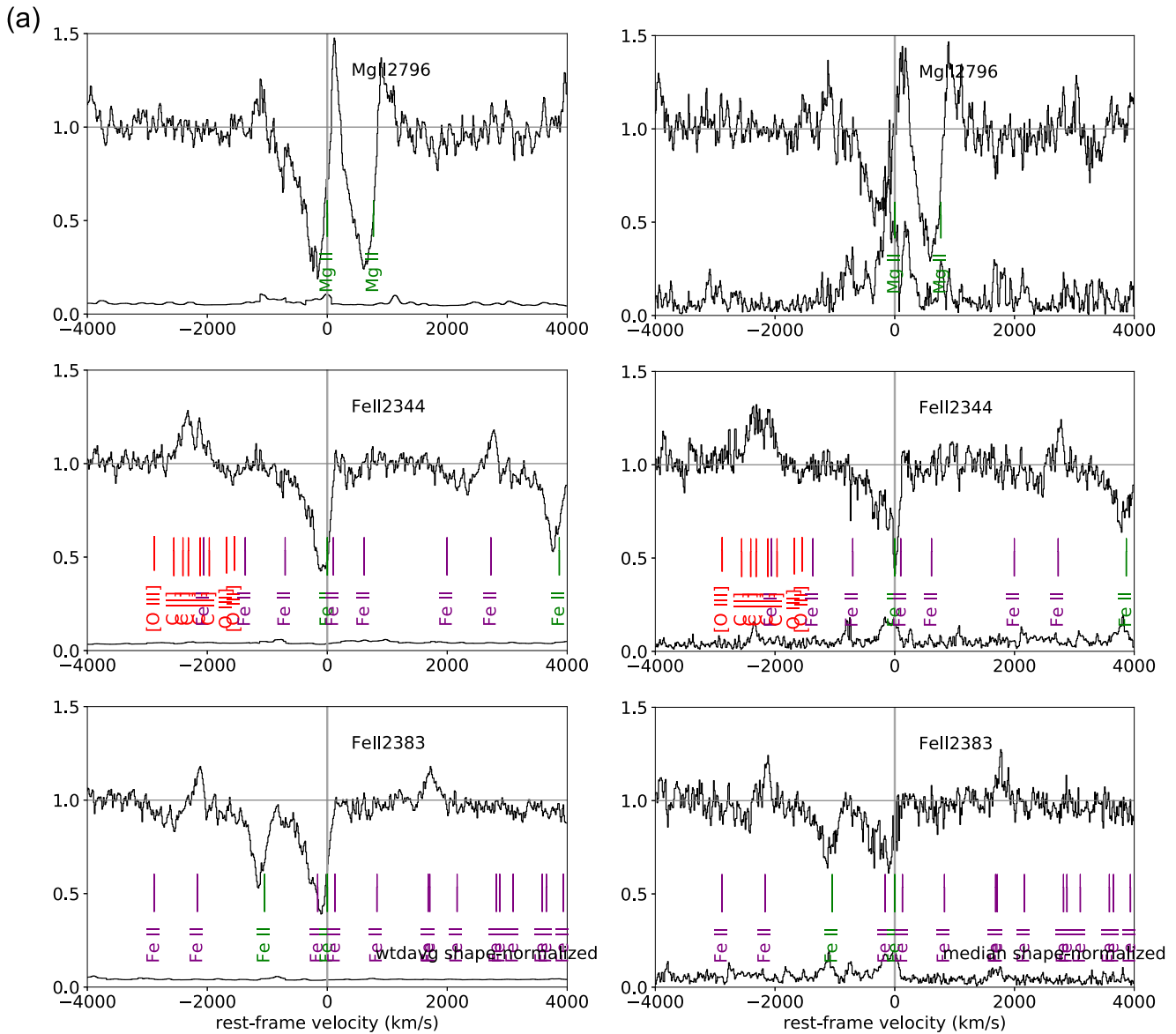


**Figure 5.** (a) The MEGA SaURA shape-normalized stacked spectrum for a weighted average (left panel) and a median (right panel) stack. Plotted is  $f_{\nu}$  vs. rest-frame velocity, with zero velocity at the systemic redshift. Because the spectra were continuum-normalized before stacking, unity represents zero absorption. Overplotted are two characterizations of the uncertainty: the propagation of the individual uncertainty spectra (left panel) and the jackknife uncertainty (right panel). Vertical ticks and labels mark the expected positions of other lines of interest, color-coded as in Figure 3. The plotted transitions trace large-scale galactic winds and have ionization potentials of 15.0 eV (Mg II) and 16.2 eV (Fe II). (b) Same as Figure 5(a), for transitions with ionization potentials from 13.6 eV (top panel) to 24.4 eV (bottom panel). The weighted average stack is shown in the left panel and the median stack in the right panel. (c) Same as Figure 5(a), for transitions with high ionization potential. Transitions are plotted in order of increasing ionization potential, from top to bottom, from 28.4 to 97.9 eV. The weighted average stack is shown in the left panel and the median stack in the right panel.

per resolution element, and the number of galaxies that went into the stack at each wavelength. The average spectral resolving power of the input spectra is  $R = 3300$ . Table 1 compares these metrics to those of composite spectra in the literature. The stacked spectra are available online in a supplemental tar.gz archive.

Figure 2 and Table 1 demonstrate that the MEGA SaURA stacked spectrum has a broader rest-frame wavelength coverage, higher S/N, and higher spectral resolution than previously published composite spectra made from starburst/LBG field galaxies (Shapley et al. 2003; Steidel et al. 2016). The subpanels of Figure 2 show that, unlike previous composites, the MEGA SaURA stack has the combination of spectral

resolution and S/N required to clearly detect faint spectral features and to measure the shapes of absorption lines. The composite MEGA SaURA spectra therefore provide the best census of rest-frame UV properties of starburst galaxies in the era of “cosmic noon”. We publicly release the MEGA SaURA composite spectra, and encourage their use as templates for understanding  $z \sim 2$  star-forming galaxies.

In Figure 3, we show the shape-normalized stack, highlighting a number of diagnostic lines, including transitions that arise variously in the ISM, nebular gas, and stellar photospheres.

For those interested in the strengths of faint emission lines, we recommend using the shape-normalized weighted average stack.

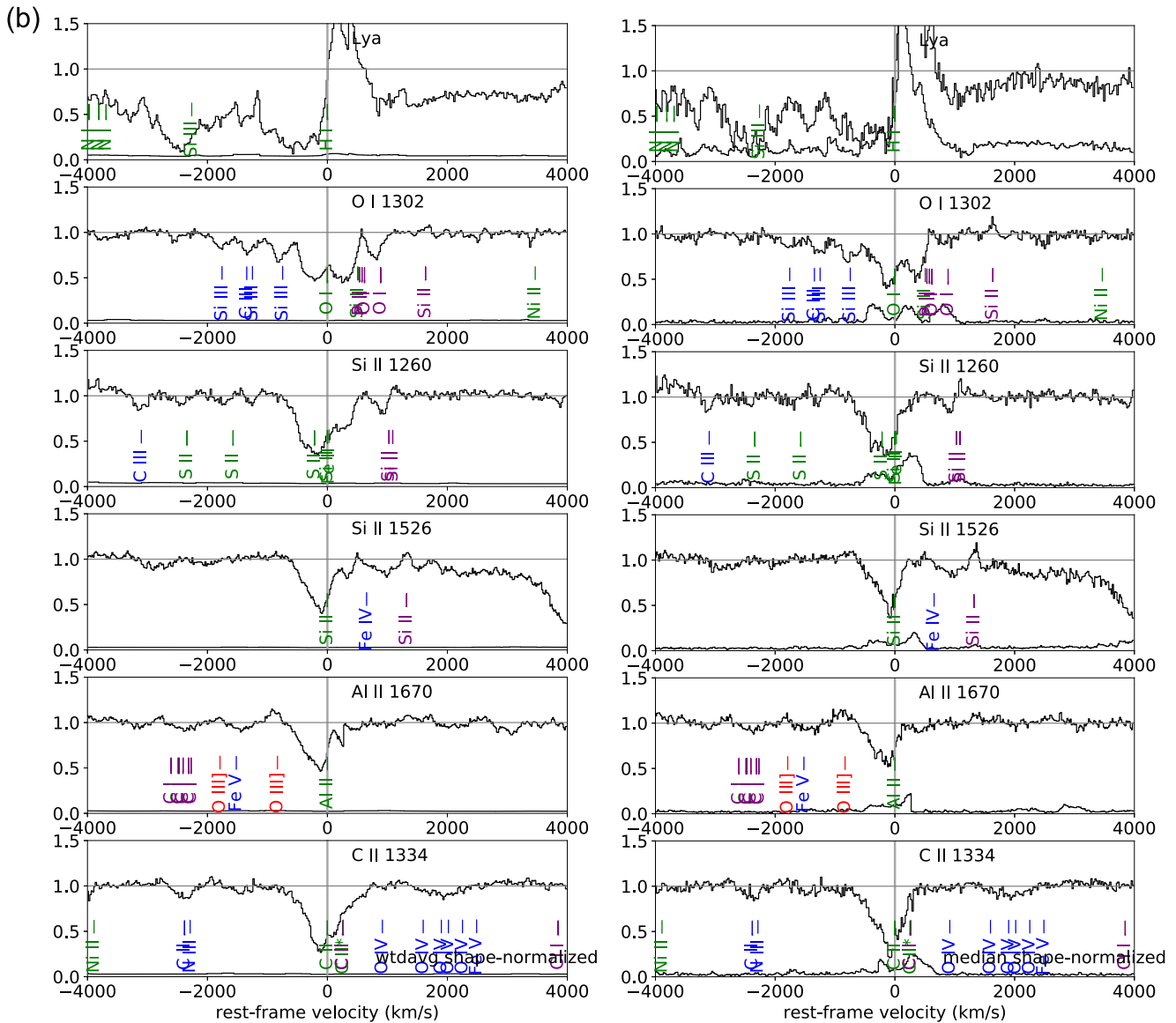


Figure 5. (Continued.)

For those interested in the overall spectral shape, we recommend using the  $\lambda_{\text{pivot}}$ -normalized weighted average stack.

### 3.2. Detected Emission Lines

Table 2 reports the equivalent width measurements for  $N = 18$  rest-frame UV emission lines detected in the MEGaSaURA shape-normalized stacked spectrum. Table 2 also reports upper limits for undetected emission lines that we expect to be generated in the ionized gas in starburst galaxies. The rest-frame UV emission lines should be useful as diagnostics of physical conditions such as the pressure of the ISM (Kewley et al. submitted to ApJ), electron temperature (D. C. Nicholls et al. 2018, in preparation), ionization parameter, metallicity, and the relative abundance pattern (Bayliss et al. 2014, L. J. Kewley et al. 2018, in preparation). By publishing the measured equivalent widths of the composite, we hope to assist observers in estimating the

integration times required to detect these lines at high redshift with *James Webb Space Telescope* (JWST).

Narrow He II 1640 Å is not detected in the stacked spectrum. However, a broad (FWHM  $\sim 2800$  km s $^{-1}$ ) excess of emission is seen over the continuum level—this may be stellar in origin. Table 2 quotes an equivalent width limit for the undetected narrow component and an equivalent width measurement for the broad component.

### 3.3. Comparison of Velocity Profiles with Low Redshift

We now consider the velocity profiles of galactic and stellar winds as seen in the stacked MEGaSaURA spectra. The MEGaSaURA stacks have the high S/N that is required to probe outflows at the highest velocities, where the absorption deficit drops to the order of a few percent of the continuum, and are of sufficient quality to enable apples-to-apples comparisons

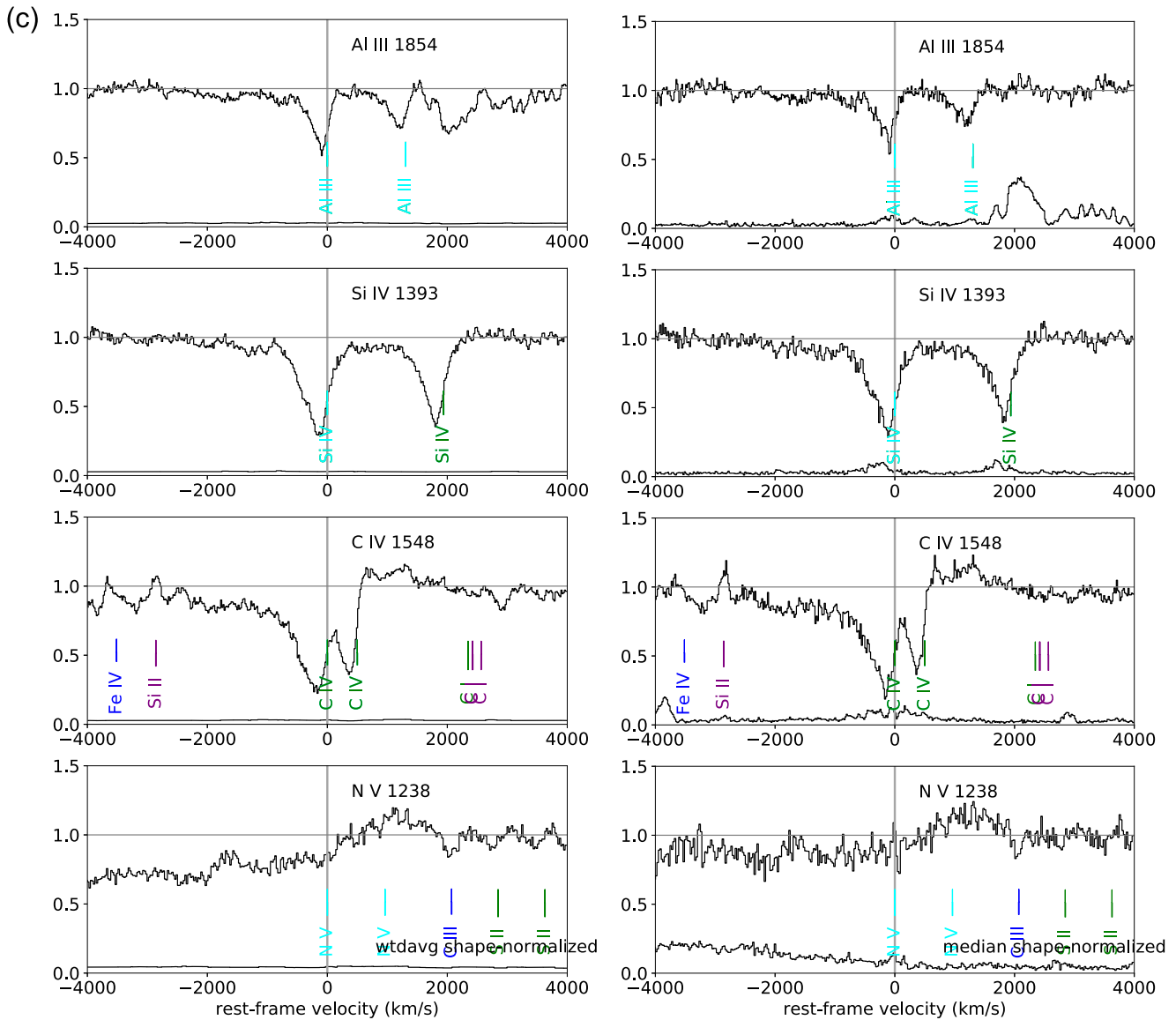


Figure 5. (Continued.)

between distant lensed starburst galaxies and some of the most vigorously star-forming galaxies in the nearby universe.

Figure 4 compares the velocity profiles of strong absorption features in two different stacks: the shape-normalized stacked spectrum of the MEGaSaURA galaxies and our stack of the  $z \sim 0$  galaxy COS spectra from Chisholm et al. (2016). The velocity profiles of the  $z \sim 2$  stack are remarkably similar to those of the  $z \sim 0$  stack, suggesting gross similarity between the galactic winds at these two very different epochs.

Table 3 quantifies this similarity; it tabulates absorption-weighted mean velocity and maximum velocity measurements for the MEGaSaURA shape-normalized stack, and for the COS/HST stack for the major absorption lines in the spectra. The next three subsections analyze the measurements in Table 3.

### 3.4. Galactic Winds as Probed by Mg II and Fe II

The wavelength coverage of the MEGaSaURA stacked spectra is sufficiently broad ( $900 < \lambda_{\text{rest}} < 3000 \text{ \AA}$ ) to cover a large number of transitions, spanning a large range of ionization potential, which can be used to characterize the

galactic and stellar winds. In Figures 5(a)–(c), we plot the absorption profiles for several absorption lines of interest.

In Figure 5(a), we consider the transitions of Mg II 2796, Fe II 2344, and Fe II 2383.<sup>12</sup> These transitions have ionization potentials of 15.0 eV (Mg II) and 16.2 eV (Fe II) and are associated with spatially resolved, large-scale outflows in galaxies at  $z \sim 1$ –2 (Martin and Bouché 2009; Weiner et al. 2009; Rubin et al. 2010, 2011; Giavalisco et al. 2011; Erb et al. 2012; Kornei et al. 2013; Bordoloi et al. 2014; Rigby et al. 2014; Rubin et al. 2014). In the MEGaSaURA weighted-average shape-normalized stack, these transitions have a maximum velocity of  $|v_{\text{max}}| = 900 \text{ km s}^{-1}$  (Table 3.)

Bordoloi et al. (2016) analyzed the velocity profiles of four regions within one of these galaxies, RCS-GA 032727–132609, and found 95th percentile velocities of 460–610  $\text{km s}^{-1}$  for these transitions. Mg II is at the extreme red end of the MEGaSaURA stack and so only four galaxy spectra went into the stack; seven galaxies contribute to the stack for Fe II 2344 and Fe II 2383.

<sup>12</sup> Fe II 2600 is unusable due to adjacent Mn II absorption.

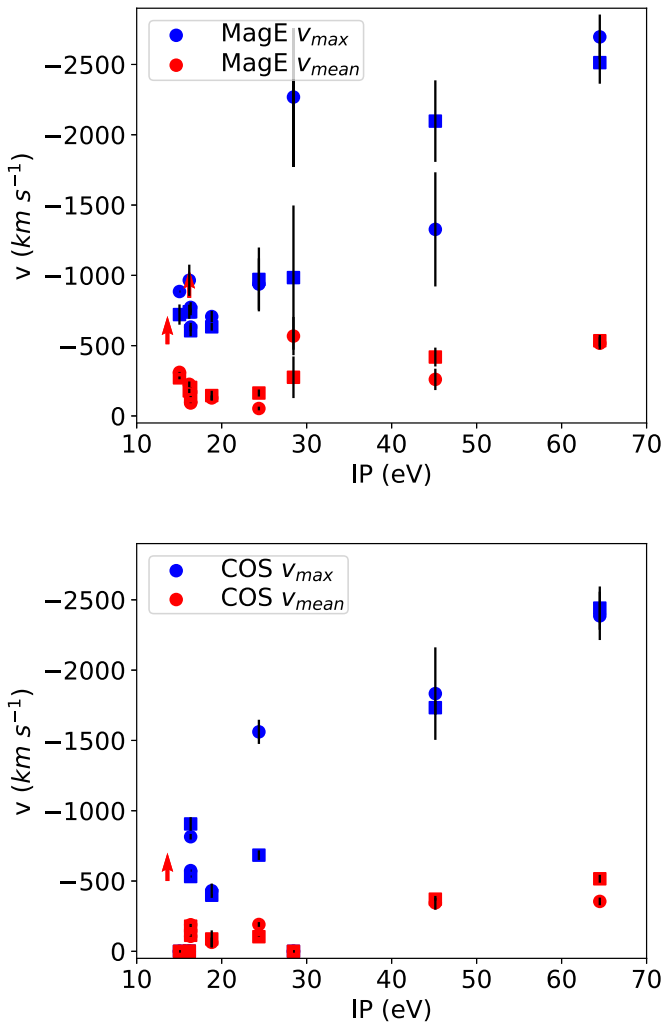


**Figure 6.** Outflow velocity vs. ionization potential. Measurements of the MEGaSaURA MagE shape-normalized stacks ( $z \sim 2$ ) are plotted in the top panel; measurements of the COS/*HST* stack ( $z \sim 0$ ) are plotted in the lower panel. In each panel, circles show measurements for the weighted-average stack and squares show measurements for the median stack. Colors differentiate two measures of the outflow velocity: the absorption-weighted mean velocity  $v_{\text{mean}}$  (red symbols) and the maximum velocity  $v_{\text{max}}$  (blue symbols).

Knot E of RCS-GA 032727–132609 contributed to the stack for both Mg II and Fe II. Despite those small numbers, the maximum velocities we measure for Mg II and Fe II confirm and extend the conclusion of Bordoloi et al. (2016): a substantial fraction of the Mg II and Fe II gas column has velocities far exceeding the plausible escape velocity of their galactic hosts.

### 3.5. Galactic Winds as Probed by Other Low-ionization Transitions

We next analyze the absorption velocity profiles of other low-ionization transitions, plotted in Figure 5(b). The main transitions that trace the neutral gas are Ly $\alpha$  and O I 1302, as they have low ionization potentials (13.6 eV). However, a maximum wind velocity cannot be measured for O I 1302 because of nearby photospheric absorption lines, and Ly $\alpha$  is difficult to interpret due to resonant scattering. Instead, we must estimate the wind velocity from Si II, Al II, and C II, which have ionization potentials of 16.3, 18.8, and 24.4 eV, respectively, and therefore trace a mixture of neutral and ionized gas. This

absorption has  $|v_{\text{max}}| \sim 630\text{--}940 \text{ km s}^{-1}$  in the MEGaSaURA weighted-average shape-normalized stack.

The maximum velocities we measure, for both the MagE and COS stacks, are comparable to the  $|v_{\text{max}}| = \sim 700\text{--}800 \text{ km s}^{-1}$  measured for Si II and C II in the composite stacked spectra of  $z \sim 2.3$  galaxies of Steidel et al. (2010) and comparable to the value of  $|v_{\text{max}}| = 900 \text{ km s}^{-1}$  measured in Si II 1260 for the  $z \sim 0$  stack of Alexandroff et al. (2015) (see Figure 1 of Heckman et al. 2015).

In Figure 6, we plot the maximum velocity (blue points) and mean velocity (red points) versus ionization potential for the MagE and COS stacks. For the low-ionization lines ( $IP < 25 \text{ eV}$ ), we find that the velocity does not strongly depend on ionization potential. Rather, the mean velocities for both samples are between  $-50$  and  $-300 \text{ km s}^{-1}$ , and the maximum velocities for both samples cluster between  $-500$  and  $-1000 \text{ km s}^{-1}$ . These results are consistent with those of Chisholm et al. (2016), who found that the overall strength of the transition, not the ionization potential, determines the measured velocity. The maximum and mean velocities are very similar between the MagE and COS samples for are very similar for each low-ionization transition. Further, the velocity profiles are very similar for these two very different epochs (see Figure 4.) We conclude that the average galactic outflow does not appreciably change from  $z \sim 2$  to  $z \sim 0$ , which suggests that similar physical processes (acceleration mechanisms, for example) establish the outflow profiles.

Thus, the galactic wind in the MEGaSaURA stacked spectrum shows a maximum blueshifted velocity that approaches but does not exceed  $1000 \text{ km s}^{-1}$ . Having established the maximum velocity of the galactic wind as traced by low ionization lines, we now examine the maximum velocities seen in high ionization transitions.

### 3.6. Stellar Winds as Probed by High-ionization Transitions

In Figure 5(c), we plot the absorption profiles of transitions with high ionization potentials, 28.4–97.9 eV. These include transitions that show classical P Cygni line profiles and are assumed to arise in stellar winds. Surprisingly weak are the emission components of N V 1238, Si IV 1393, and C IV 1548. The weakness of this emission indicates that Wolf Rayet stars and/or the most massive O stars are present, but rare.

We consider the absorption profiles of these high ionization lines. N V 1238 is difficult to measure given the complexity of the continuum near Ly $\alpha$ . C IV 1548, Si IV 1393, and Al III 1854 all show similar velocity profiles: strong absorption at velocities close to systemic, presumably from the ISM, as well as a blueshifted absorption tail extending to  $|v_{\text{max}}| = 1300\text{--}2700 \text{ km s}^{-1}$ . In C IV, this blueshifted absorption tail is detectable in individual MEGaSaURA spectra with high S/N, namely RCS-GA 032727–132609, SGAS J010842.2+062444, SGAS J003341.5+024217, SGAS J090003.3+223408, the Cosmic Horseshoe, and SGAS J152745.1+065219.

Al III 1854, with an ionization potential of 28.4 eV, is variously considered in the literature to be either an ISM or a stellar wind line. In the stacked spectrum, the high  $|v_{\text{max}}|$  and shape of its high-velocity tail strongly suggest that at least a substantial portion of Al III 1854 absorption has a similar origin to C IV and Si IV. This is supported by the fact that Al III 1854 has been observed with a P Cygni profile in certain B supergiants of spectral and luminosity classes: B0.7 Ia to B2.5 Ia; B1–B3 Ia+ /Iap; and BC1.5 Iab (Walborn et al. 1995).

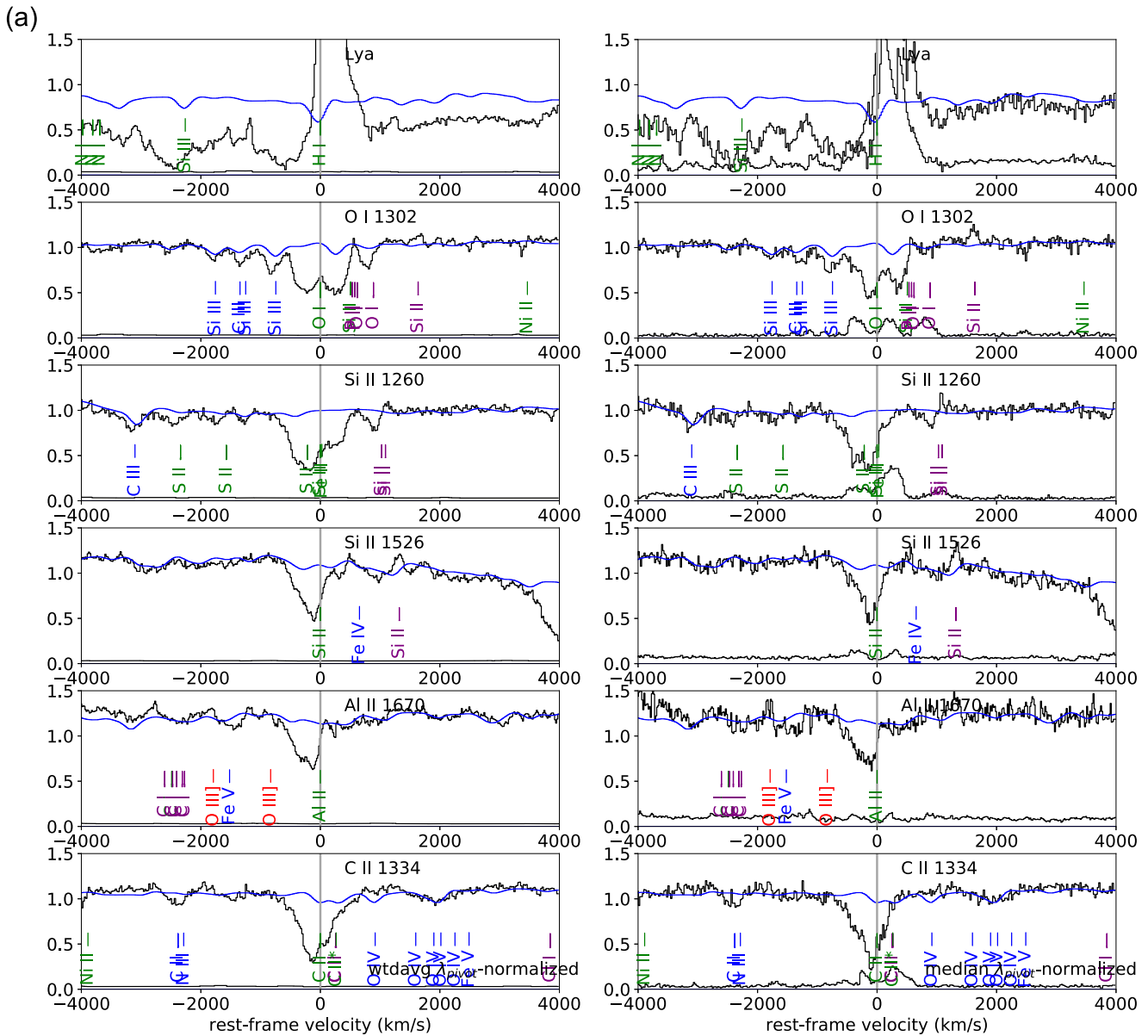


**Figure 7.** (a) The MEGA SaURA  $\lambda_{\text{pivot}}$ -normalized stacked spectrum (in black), compared to the best-fit Starburst99 stellar continuum (blue). Transitions plotted are as in Figure 5(a), for the weighted average (left panel) and median (right panel) stacks. (b) Same as Figure 7(b), for high ionization potential transitions, for the weighted average (left panel) and median (right panel) stacks. The S99 fit reproduces the blue wing of the C IV absorption fairly well; it does a poorer job reproducing the N V feature and the blue wing of the Si IV feature. The poor fit blueward of N V 1238 is due to broad Ly $\alpha$  absorption and H $_2$  extinction.

Thus, the Al III profile further underscores the large contribution to the spectra from B stars.

In Figure 6, we plot the maximum and mean velocities of the high-ionization absorption lines. For both the MagE and COS samples, there is a trend where the maximum velocities increase with increasing ionization potential, but the absorption-weighted mean velocities remain nearly constant for all ionization potentials. This indicates that the high-ionization lines have a weak blue-velocity tail extending to more than  $\sim 2000 \text{ km s}^{-1}$ , but that the majority of the absorption has similar velocities to the low-ionization gas. This supports our hypothesis that the blue-velocity wings arise in the hot photospheres of massive stars, while the stronger absorption component at redder velocities arises from a multi-phase galactic outflow. Properly accounting for the stellar winds is important when measuring the maximum outflow velocities of high-ionization lines.

The absorption in this high-velocity tail is only 6%–10% below the continuum level for Al III and Si IV and only 15% for C IV. As such, detecting it requires high S/N spectra like those of the MEGA SaURA stacked spectrum. This high-velocity absorption tail *is not seen* in the profiles of transitions with lower ionization potential, as quantified in Sections 3.4 and 3.5. This correspondence supports our hypothesis that the blue absorption wings of the high ionization lines are likely due to the stellar winds of massive stars.

### 3.7. Stellar Winds Fit by Stellar Population Synthesis

We now consider the extent to which Starburst99 stellar population synthesis models can reproduce these high-velocity stellar wind features. Thus far, we have considered the shape-normalized stack, which minimizes undesirable ringing and is therefore ideal to study these low level features. However, for

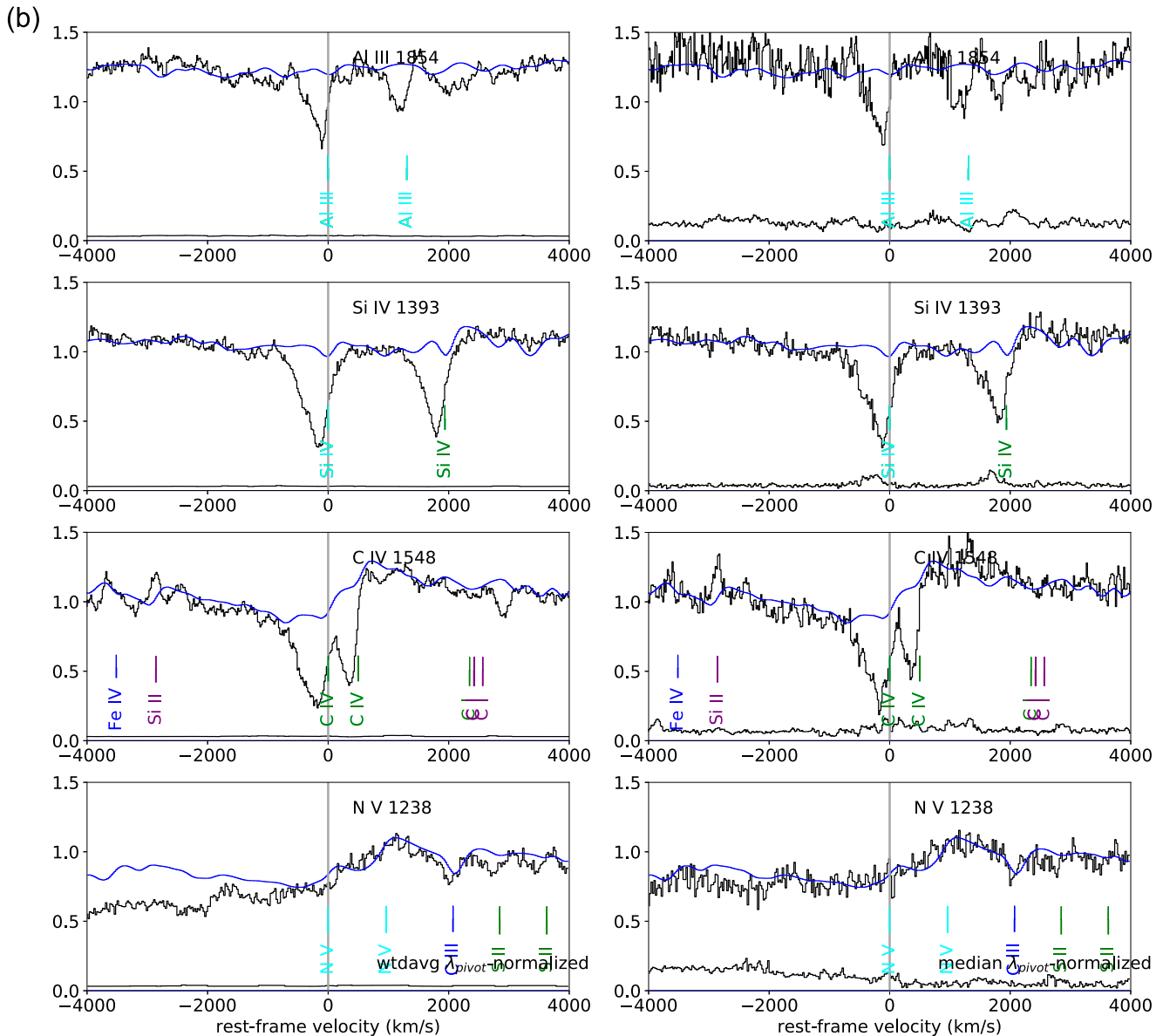


Figure 7. (Continued.)

spectral synthesis fitting, we use the  $\lambda_{\text{pivot}}$ -normalized stack, as it preserves the spectral shape. We plot the low-ionization features in the  $\lambda_{\text{pivot}}$ -normalized stack in Figure 7(a) and the high-ionization features in Figure 7(b). For both Figures 7(a) and (b), we overplot the best-fitting linear combination of Starburst99 models. The Starburst99 fit decently matches the N V, Si IV, and C IV emission features, as well as the high-velocity tail of C IV.

As a cross-check, we examine the profiles of these stellar wind lines in the S99-normalized stack. Because each input spectrum was continuum-normalized by its Starburst99 fit before stacking, the S99-normalized stack provides a different way to test whether the Starburst99 models can match the the observed high-velocity absorption profiles. Figure 8 shows negligible residual absorption at high velocities, indicating that the Starburst99 models can indeed reproduce the high-velocity tail of absorption from stellar winds.

#### 4. Discussion and Conclusions

We have stacked the MagE/Magellan spectra of  $N = 14$  gravitationally lensed galaxies from Project MEGaSaURA

(Paper I), to produce a new spectral composite of star-forming galaxies at redshift  $z \sim 2$ , one with the requisite high signal-to-noise, moderate spectral resolution, and wavelength coverage that are needed to constrain the massive star populations and the kinematics of outflowing gas. We publish electronic versions of the MEGaSaURA stacked spectra (Section 3.1) to encourage their use by the scientific community.

We detect  $N = 18$  rest-frame UV emission lines in the MEGaSaURA stack. These include relatively strong lines—[C III] 1907, [C III] 1909 Å, and Mg II 2796, 2803 Å with  $W_r \sim 0.5$  Å—as well as weaker lines of He II, C II, N II, [O II] and [O III], Si II and Si III, and Fe II. We publish equivalent widths for these lines to assist in estimating spectroscopic exposure times for JWST.

To enable consistent comparison between galaxies in the distant universe and the local universe, we stack the COS/HST spectra of  $z \sim 0$  galaxies with outflows, with the spectral resolution downgraded to approximately that of MagE. We publish this stack COS/HST as well. A surprising result from



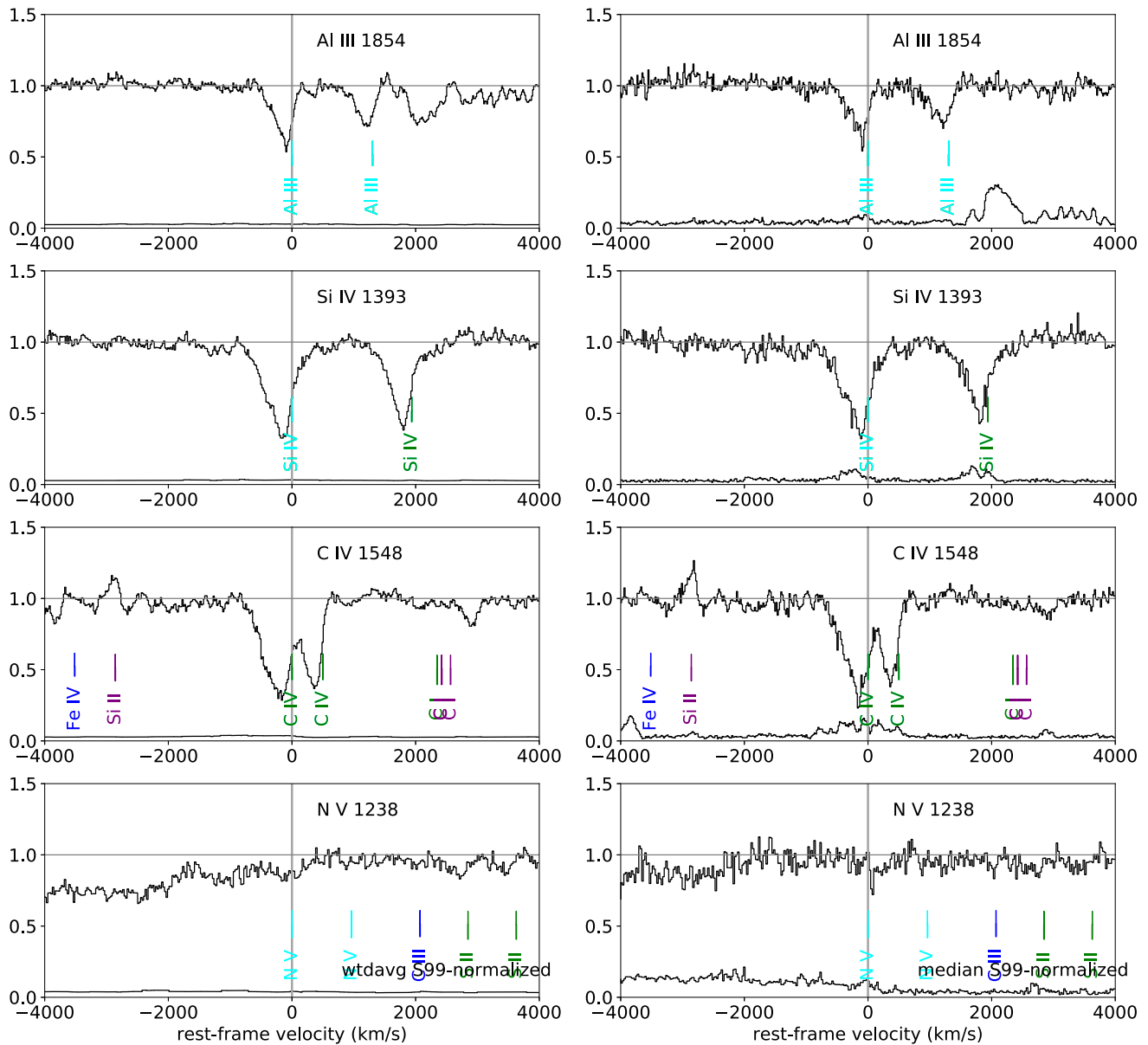


**Figure 8.** The S99-normalized stack, for transitions with high ionization potential, for the weighted average (left panel) and median (right panel) stacks. The profiles show negligible absorption at high velocities, which confirms that the best-fit Starburst99 models are able to reproduce the stellar winds.

this work is how similar the outflow velocity profiles in the  $z \sim 2$  MagE stack and in the  $z \sim 0$  COS/*HST* stack are to one another. This similarity suggests that similar physical processes may be driving the outflows at both epochs. We plan to follow up this result by examining the outflows on a galaxy-by-galaxy basis using the individual MEGaSaURA spectra.

In the MEGaSaURA composite, the absorption-weighted mean velocities are similar for ions of low and high ionization potential, which indicates that most of the highly ionized gas is part of the multi-phase outflow that is traced by the low-ionization absorption lines. Very similar behavior is seen in our stack of  $z \sim 0$  galaxy spectra from COS/*HST*. For both the  $z \sim 2$  MagE stack and the  $z \sim 0$  COS stack, the high ionization lines show a blue tail of absorption, with maximum velocity of up to  $-2700 \text{ km s}^{-1}$  and  $-1300 \text{ km s}^{-1}$  in the wings of C IV 1548 and Si IV 1393, respectively, for the MagE stack, and  $-2400 \text{ km s}^{-1}$  and  $-1800 \text{ km s}^{-1}$  for the COS stack.

At velocities above  $-1000 \text{ km s}^{-1}$ , the absorption is only 6%–15% of the continuum, and therefore requires high signal-to-noise to be detectable. This high-velocity absorption tail is not seen in the profiles of transitions that trace neutral and low-ionization gas. The most plausible explanation is that this high-velocity tail is a stellar wind feature originating from the regions around hot stars. Using two different methodologies, we confirm that linear combinations of current Starburst99 models are able to reproduce this blue tail of high-velocity absorption in the MagE stack. As improvements are made to stellar population synthesis models, they will need to demonstrate that they, too, can reproduce this high-velocity absorption tail.

While the Starburst99 fitting is able to reproduce the overall continuum shape of the MEGaSaURA  $\lambda_{\text{pivot}}$ -normalized stack as well as the P Cygni stellar wind features, it does not adequately reproduce some of the photospheric absorption features. This is




clearly seen in the second panel and the last panel of Figure 7(a), where a complex of C III and Si III lines at  $\lambda_{\text{rest}} = 1296 \text{ \AA}$  and a blend of C II and N III at  $\lambda_{\text{rest}} = 1324 \text{ \AA}$  are poorly matched by the Starburst99 fitting. These rest-frame ultraviolet photospheric absorption lines provide an additional set of constraints to population synthesis models; we will examine them in more detail in a future paper.

The composite spectrum presented in this paper is timely, as we are about to enter a golden age for rest-frame ultraviolet astronomy. The Near Infrared Spectrograph (NIRSpec) on board *JWST* will soon detect the strongest of these rest-frame ultraviolet diagnostics in galaxies out to extremely high redshifts. For example, the [C III] 1907, C III] 1909  $\text{\AA}$  emission-line doublet and the C IV 1548, 1551  $\text{\AA}$  doublet are redshifted into the NIRSpec range for redshifts of  $z \gtrsim 2.2$  and  $z \gtrsim 3.0$ , respectively. With sufficiently deep integrations, *JWST* should capture these and other ultraviolet diagnostics out to redshifts as high as galaxies can be found. Templates, like the composite presented here, will be necessary to interpret these *JWST* spectra, especially at the highest redshifts, where only a few of the brightest emission lines will probably be obtained.

We thank the staff of Las Campanas Observatories for their dedicated service, which made possible these observations. We thank the telescope allocation committees of the Carnegie Observatories, The University of Chicago, The University of Michigan, and Harvard University, for granting observing time to this observing program over several years. We thank A. Shapley, C. Steidel, G. Zhu, and M. Pettini for making available electronic versions of their spectra. R.B. was supported by NASA through Hubble Fellowship grant #51354 awarded by the Space Telescope Science Institute, which is operated by the Association of Universities for Research in Astronomy, Inc., for NASA, under contract NAS 5-26555. We thank the referee for thoughtful suggestions that improved the paper.

#### ORCID iDs

J. R. Rigby  <https://orcid.org/0000-0002-7627-6551>  
 M. B. Bayliss  <https://orcid.org/0000-0003-1074-4807>  
 J. Chisholm  <https://orcid.org/0000-0002-0302-2577>  
 R. Bordoloi  <https://orcid.org/0000-0002-3120-7173>  
 K. Sharon  <https://orcid.org/0000-0002-7559-0864>

T. Johnson  <https://orcid.org/0000-0002-8829-5303>  
 E. Wuyts  <https://orcid.org/0000-0002-4105-3315>  
 H. Dahle  <https://orcid.org/0000-0003-2200-5606>

#### References

- Alexandroff, R. M., Heckman, T. M., Borthakur, S., Overzier, R., & Leitherer, C. 2015, *ApJ*, **810**, 104
- Bayliss, M. B., Rigby, J. R., Sharon, K., et al. 2014, *ApJ*, **790**, 144
- Bordoloi, R., Lilly, S. J., Hardmeier, E., et al. 2014, *ApJ*, **794**, 130
- Bordoloi, R., Rigby, J. R., Tumlinson, J., et al. 2016, *MNRAS*, **458**, 1891
- Cardelli, J. A., Clayton, G. C., & Mathis, J. S. 1989, *ApJ*, **345**, 245
- Chisholm, J., Tremonti, C. A., Leitherer, C., et al. 2015, *ApJ*, **811**, 149
- Chisholm, J., Tremonti, C. A., Leitherer, C., Chen, Y., & Wofford, A. 2016, *MNRAS*, **457**, 3133
- Crowther, P. A., Caballero-Nieves, S. M., Bostroem, K. A., et al. 2016, *MNRAS*, **458**, 624
- Dalcanton, J., Seager, S., Aigrain, S., et al. 2015, arXiv:1507.04779
- Erb, D. K., Quider, A. M., Henry, A. L., & Martin, C. L. 2012, *ApJ*, **759**, 26
- Giavalisco, M., Vanzella, E., Salimbeni, S., et al. 2011, *ApJ*, **743**, 95
- Green, G. M., Schlafly, E. F., Finkbeiner, D. P., et al. 2015, *ApJ*, **810**, 25
- Heckman, T. M., Alexandroff, R. M., Borthakur, S., Overzier, R., & Leitherer, C. 2015, *ApJ*, **809**, 147
- Heckman, T. M., Borthakur, S., Overzier, R., et al. 2011, *ApJ*, **730**, 5
- Jones, T., Stark, D. P., & Ellis, R. S. 2012, *ApJ*, **751**, 51
- Kinney, A. L., Bohlin, R. C., Calzetti, D., Panagia, N., & Wyse, R. F. G. 1993, *ApJS*, **86**, 5
- Kornei, K. A., Shapley, A. E., Martin, C. L., et al. 2013, *ApJ*, **774**, 50
- Kouveliotou, C., Agol, E., Batalha, N., et al. 2014, arXiv:1401.3741
- Leitherer, C., Ortíz Otálvaro, P. A., Bresolin, F., et al. 2010, *ApJS*, **189**, 309
- Leitherer, C., Schaerer, D., Goldader, J. D., et al. 1999, *ApJS*, **123**, 3
- Leitherer, C., Tremonti, C. A., Heckman, T. M., & Calzetti, D. 2011, *AJ*, **141**, 37
- Marshall, J. L., Burles, S., Thompson, I. B., et al. 2008, *Proc. SPIE*, **7014**, 701454
- Martin, C. L., & Bouché, N. 2009, *ApJ*, **703**, 1394
- Meynet, G., Maeder, A., Schaller, G., Schaerer, D., & Charbonnel, C. 1994, *A&AS*, **103**, 97
- Rigby, J. R., Bayliss, M. B., Gladders, M. D., et al. 2014, *ApJ*, **790**, 44
- Rubin, K. H. R., Prochaska, J. X., Koo, D. C., et al. 2014, *ApJ*, **794**, 156
- Rubin, K. H. R., Prochaska, J. X., Ménard, B., et al. 2011, *ApJ*, **728**, 55
- Rubin, K. H. R., Weiner, B. J., Koo, D. C., et al. 2010, *ApJ*, **719**, 1503
- Schneider, D. P., Hartig, G. F., Jannuzi, B. T., et al. 1993, *ApJS*, **87**, 45
- Shapley, A. E., Steidel, C. C., Pettini, M., & Adelberger, K. L. 2003, *ApJ*, **588**, 65
- Steidel, C. C., Erb, D. K., Shapley, A. E., et al. 2010, *ApJ*, **717**, 289
- Steidel, C. C., Strom, A. L., Pettini, M., et al. 2016, arXiv:1605.07186
- Walborn, N. R., Parker, J. W., & Nichols, J. S. 1995, VizieR On-line Data Catalog: III/188, 1363
- Weiner, B. J., Coil, A. L., Prochaska, J. X., et al. 2009, *ApJ*, **692**, 187
- Wuyts, E., Rigby, J. R., Gladders, M. D., et al. 2012, *ApJ*, **745**, 86
- Zhu, G. B., Comparat, J., Kneib, J.-P., et al. 2015, *ApJ*, **815**, 48